Electrically controlled charge qubit in van der Waals heterostructures: From *ab initio* calculation to tight-binding models

Gusthavo M. S. Brizolla ,[*] A. J. Chaves , L. K. Teles, and I. Guilhon[†]

Grupo de Materiais Semicondutores e Nanotecnologia, Instituto Tecnológico de Aeronáutica,
DCTA, 12228-900 São José dos Campos, Brazil

J. M. Pereira Junior

Grupo de Teoria da Matéria Condensada, Departamento de Física, Universidade Federal do Ceará,
60455-760 Fortaleza, Ceará, Brazil

Quantum computing demands innovative approaches for realizing qubits, and one promising avenue involves leveraging gated hybridized van der Waals (vdW) vertical heterostructures, referred to as vdW qubits. The two-level system that characterizes the vdW qubit comes from the layer-dependent orbital character of the charge carrier. This paper investigates the potential of gated vdW heterostructures for quantum computing. We study how gate fields affect the orbital composition of bands, enabling spatial superposition of electrons across layers of two-dimensional materials. Our *ab initio* calculations assess 20 transition metal dichalcogenides, identifying layers with slight energy offsets as vdW qubit candidates. Our investigation extends to the heterostructures formed based on the layered materials meeting these criteria. To simulate these qubits within large quantum circuits efficiently, we employ the tight-binding approach with maximally localized Wannier functions, validated against full *ab initio* calculations. At zero field, we confirm the existence of highly hybridized states that manifest as a qubit state exhibiting an approximately equal distribution between $|0\rangle$ and $|1\rangle$. The electric field application serves as a modulator for adjusting the contribution of these states. This phenomenon is general and is explored in the context of four distinct heterostructures. In addition, our study identified 222 possible combinations matching different layers on the conduction or the valence as promising host heterostructures for implementing vdW qubits.

I. INTRODUCTION

Since the early 1980s, quantum computing has become a topic of great interest, stemming from the seminal discussions initiated by Richard Feynman [1]. Feynman's musings on utilizing computers to simulate complex physics problems brought forth the intriguing potential of those machines. He envisioned a computer capable of precisely emulating natural processes, surpassing the capabilities of classical computers, at the same time being universal, in the sense of solving any problem and not specific ones. This concept of universality of such a machine was further elaborated by David Deutsch [2]. Presently, quantum computing not only offers the capability to solve intricate problems but also serves as a testing ground for the fundamental principles of quantum mechanics itself [3].

In order to create a functional quantum computer, it becomes necessary to manipulate interconnected qubits, which are the building blocks of quantum circuits. Qubits can be physically implemented in different ways, such as by means of superconductors [4–6], electronic and nuclear spin degree of freedom [7,8], trapped ions [9,10], molecules [11,12], as well as by exploiting topological properties of solid state systems [13], with each of these implementations offering distinct capabilities and challenges.

The application of semiconductor-based qubits has attracted significant interest due to their compatibility with concepts from the microelectronics industry [14,15]. Current research is dedicated to exploring physical implementations of materials that show potential for integration into quantum chips capable of operating with numerous logical qubits, thus driving advancements in large-scale quantum integration. The remarkable diversity of properties exhibited by two-dimensional (2D) materials, along with their high versatility at the nanometer scale, makes them promising candidates for quantum circuits, which can lead to advancements in the field of quantum information [16,17]. Due to their distinctive attributes, 2D materials have emerged as promising candidates for qubit development [18,19]. Transition metal dichalcogenides (TMDs), in particular, exhibit intriguing structural and electronic properties that render them suitable for such applications. Furthermore, high-performance transistors and optoelectronic devices based on graphene and TMDs have been explored [20,21]. Moreover, the capacity to manipulate the electronic properties of 2D materials through external stimuli, such as electric fields [22], strain [23–25], and doping [26], provide novel avenues for tailoring their characteristics to meet specific application requirements.

Recently, an innovative proposal has emerged, namely the use of gated van der Waals (vdW) heterostructures as charge

*gusthavomsbrizolla@gmail.com
†guilhon@ita.br

qubits, henceforth referred to as vdW qubits [27]. The interlayer environment is characterized by weak covalent bonds that stabilize the hole structure allowing the formation of numerous stacking combinations [28]. These solid-state systems exhibit collective behavior and their properties can be easily manipulated through external perturbations, such as electric fields, presenting significant potential for revolutionizing quantum computing.

This qubit arises from the quantum superposition of states within the constituent materials of the vdW heterostructure. This superposition is achieved by pairing materials exhibiting minimal energy differences in their valence band maximum and conduction minimum concerning the vacuum level. Several prior studies have delved into the investigation of energy levels in layered materials through *ab initio* calculations, aiming to identify heterostructures tailored for specific technological applications [29–31]. Here the resultant slight energy mismatch enables the emergence of the desired hybridization in the band structure, defining the fundamental two-level system inherent to the vdW qubit concept.

This innovative proposal explores the orbital composition of the bands at a given k point as a function of the gate field, allowing for the achievement of spatial superposition of electrons from individual layers. The vast number of possible combinations of 2D materials makes this proposal a promising avenue for further exploration.

Simulating realistic devices at the full *ab initio* level can be computationally challenging, especially for large systems. In such cases, tight-binding Hamiltonian models (TBH) provide an alternative approach for tackling the electronic structure problem, enabling simulations of large systems. These models can be parametrized by fitting procedures or machine learning models to reproduce accurate first-principles calculations. For monolayers of TMDs, tight-binding (TB) models using only d orbitals accurately reproduce low-energy bands through fitting procedures based on *ab initio* calculations [32]. Machine learning has also been explored for obtaining TB parameters for defect simulations [33]. Realistic descriptions of large-scale models for black phosphorus, derived from GW_0 calculations, have successfully replaced computationally intensive calculations with simple TB models [34]. Another approach for describing TMDs' band structure involves creating a TBH based on Bloch wave functions and mapping them into Wannier functions (WFs). This approach succeeded by using d orbitals of the metal and p orbitals of the chalcogen as WFs, considering interactions up to first and second neighbors, and interlayer interactions mediated by the chalcogen's p orbitals [35].

This work presents an *ab initio* TB model for vdW heterostructures of TMDs obtained from density functional theory (DFT) calculations using hybrid functional, without relying on fitting procedures or empirical parameters. The model, constructed from localized d and p orbitals, includes the first- and second-neighbor couplings, and we can safely neglect higher orders due to exponential decay, usually sufficient for understanding the nature of the bands. Adding more terms beyond nearest-neighbor couplings can improve accuracy, eventually approaching results comparable to those obtained from the *ab initio*. The objective in obtaining such a model aims to analyze the electric control of the vdW qubit's

TABLE I. Cutoff energy for the plane-wave expansion (E_{cut}) and the mesh of k points (k-mesh) that assures well converged DFT with respect to the total energy. T and H stand for the allotropic form.

TMDs	E_{cut} (Ry)	k-mesh
HfS_2 (T)	160	$10 \times 10 \times 1$
HfS_2 (H)	120	$10 \times 10 \times 1$
$HfSe_2$ (T)	180	$12 \times 12 \times 1$
$HfSe_2$ (H)	120	$10 \times 10 \times 1$
MoS_2 (T)	160	$10 \times 10 \times 1$
MoS_2 (H)	160	$10 \times 10 \times 1$
$MoSe_2$ (T)	160	$14 \times 14 \times 1$
$MoSe_2$ (H)	160	$10 \times 10 \times 1$
SnS_2 (T)	120	$10 \times 10 \times 1$
SnS_2 (H)	120	$10 \times 10 \times 1$
$SnSe_2$ (T)	140	$12 \times 12 \times 1$
$SnSe_2$ (H)	120	$12 \times 12 \times 1$
WS_2 (T)	140	$10 \times 10 \times 1$
WS_2 (H)	160	$10 \times 10 \times 1$
WSe_2 (T)	160	$14 \times 14 \times 1$
WSe_2 (H)	120	$10 \times 10 \times 1$
ZrS_2 (T)	120	$10 \times 10 \times 1$
ZrS_2 (H)	120	$10 \times 10 \times 1$
$ZrSe_2$ (T)	140	$12 \times 12 \times 1$
$ZrSe_2$ (H)	120	$10 \times 10 \times 1$

orbital character, once an electric field acts perturbatively in the onsite energies and then compare results with DFT calculations to verify the accuracy of the model.

The article is organized as follows: In Sec. II, we describe the systems and the methods adopted in our calculations. In Secs. III and IV, we present and discuss the results. Finally, in Sec. V, we briefly summarize the paper.

II. METHODS

A. *Ab initio* calculations

The structural and electronic properties are calculated using the DFT formalism [36,37] as implemented in the Quantum ESPRESSO [38–40] package. For the monolayers of TMDs, cutoff energy for the plane-wave expansion ranging from 120 to 160 Ry was used due to the structural and electronic properties of the allotropes considered, and the integrations over the Brillouin zone (BZ) have used a Monkhorst-Pack mesh for k-point sampling [41]. Table I gives the value used for each material.

The atomic positions were relaxed until a convergence threshold of 10^{-5} Ry/bohr on the forces and 10^{-5} Ry on the energy. The SCF cycle's convergence threshold was 10^{-8} Ry. A vacuum of 30 Å was used to avoid spurious interactions of the periodic images for the monolayers with truncation of the Coulomb interaction perpendicular to the slab [42]. Heterostructure investigations are performed after obtaining relaxed lattice parameters of each monolayer and applying necessary strains, in which for all the systems here discussed was smaller than 1%, to make the systems commensurate. The same vacuum in the stacking direction was employed.

The wave functions and pseudopotentials are generated within the scalar-relativistic optimized norm-conserving

Vanderbilt pseudopotential code [43–45] taken from The PseudoDojo project [46]. Exchange and correlation (XC) are described using the Perdew-Burke-Ernzerhof [47,48]. To describe excited states more accurately, and consequently the energy levels more accurately, the hybrid functional HSE06 [49–51] was employed, making use of the adaptively compressed exchange [52], which greatly reduces the computational cost associated with the Fock exchange operator without loss of accuracy. With the use of HSE06, the divergence of the coulomb potential for small q vectors on the Fock grid is handled by the treatment of Gygi and Baldereschi [53]. During the DFT calculation, the sawtooth electrostatic potential was utilized to implement the electric field, as discussed in Refs. [54,55]. The vdW interaction, where the vdW-DF family was implemented by the Thonhauser group [56–58], used was vdW-DF-obk8 [59].

B. Maximally localized Wannier functions

A localized description of the Bloch eigenfunctions can be obtained from a Fourier transform of the form [60]

$$w_n(\mathbf{r}) = \frac{V}{(2\pi)^3} \int_{BZ} \psi_{n\mathbf{k}}(\mathbf{r}) e^{-i\mathbf{k}\cdot\mathbf{R}} d\mathbf{k}, \tag{1}$$

where $w_n(\mathbf{r})$ is the nth WF, $\psi_{n\mathbf{k}}(\mathbf{r})$ are the Bloch states, V is the volume of the unit cell, k is the quasimomentum quantum number, $\mathbf{R}$ are the lattice vectors, and the integral is over the first BZ with n being the band index. Moreover, this transformation has gauge freedom since the Bloch states do not change when multiplied by a phase factor. In general, for a case of composite bands, one has the freedom to mix them with a unitary transformation $U_{mn}^{(\mathbf{k})}$, such as

$$w_n(\mathbf{r}) = \frac{V}{(2\pi)^3} \int_{BZ} \left[\sum_m U_{mn}^{(\mathbf{k})} \psi_{n\mathbf{k}}(\mathbf{r}) \right] e^{-i\mathbf{k}\cdot\mathbf{R}} d\mathbf{k}, \tag{2}$$

with $U_{mn}^{(\mathbf{k})}$ being unitary matrices that mix the Bloch states. A recipe for the localization procedure of WFs was proposed based on minimizing a functional that measures the real space spread of such functions [61,62], dealing with the gauge freedom that comes from the unitary matrix $U_{mn}^{(\mathbf{k})}$, redefining such transformation in order to satisfy the criterion, as implemented in the Wannier90 package [63–65]. The spread functional to be minimized is given by

$$\Omega = \sum_n \left[\langle r^2 \rangle_n - \bar{\mathbf{r}}_n^2 \right], \tag{3}$$

with

$$\bar{\mathbf{r}}_n = i \frac{V}{(2\pi)^3} \int d\mathbf{k} \langle u_{n\mathbf{k}} | \nabla_{\mathbf{k}} | u_{n\mathbf{k}} \rangle, \tag{4}$$

$$\langle r^2 \rangle_n = \frac{V}{(2\pi)^3} \int d\mathbf{k} | |\nabla_{\mathbf{k}} u_{n\mathbf{k}} \rangle |^2, \tag{5}$$

in which the MLWFs are obtained by minimizing Eq. (3) with respect to $U_{mn}^{(\mathbf{k})}$. Here $|u_{n\mathbf{k}}\rangle$ are the periodic part of the Bloch states. This functional can be written as a sum of two quantities,

$$\Omega = \Omega_I + \tilde{\Omega}, \tag{6}$$

where the first term is gauge independent, and the latter is gauge dependent [61]. Now, since the expectation values in Eq. (3) involve the position operation, it is necessary to rewrite the necessary expressions in k space, something that can be achieved with the help of the Blount identities [66]. All the desired quantities derived in Ref. [61] for the spread functional depend only on the overlap between the periodic part of the Bloch states,

$$M_{m,n}^{(\mathbf{k},\mathbf{b})} = \langle u_{m\mathbf{k}} | u_{n,\mathbf{k}+\mathbf{b}} \rangle. \tag{7}$$

Such overlaps can be obtained from the *ab initio* calculations and will be the main input for the Wannier90 code.

This Wannierization procedure may potentially break the symmetry of the orbitals and consequently the symmetry of our Hamiltonian. The symmetries play a crucial role, especially when dealing with noncollinear simulations of nonmagnetic materials influenced by spin-orbit coupling, many-body techniques exploring topological effects, as detailed in a recent publication [67]. However, this usual Wannierization procedure approximately adheres to symmetry conditions, with changes in the band-structure interpolation on the order of submillielectronvolt [68]. Furthermore, consideration of unoccupied bands enables the MLWFs to achieve greater localization, thereby restoring some symmetries that might otherwise be compromised [69]. Given our primary focus on accurate band interpolation and agreement with the DFT band structure, this approach proves sufficient for effectively modeling the systems under investigation.

C. Tight-binding model

The TB parameters obtained are solely determined by the overlap integrals for orbitals and the matrix elements from the full *ab initio* calculation. The WFs corresponding to the initial guesses are based on a projected band structure in the atomic orbitals analysis, used to determine the resulting sparse Hamiltonian. Although the real-space Hamiltonian has low dimensionality, its matrix elements (hopping parameters) decay slowly with distance, leading to a large number of small parameters. In order to make the resulting model more tractable, we ignore parameters beyond the cutoff radius $|d_{hop}|$ restricting the model to hoppings between first and second neighbors. The truncation of the sparse Hamiltonian was performed using the PythTB program to obtain the best fidelity to the DFT results regarding band structure, band gap, and orbital character.

Moreover, in our TB model, we introduced an unscreened electric field represented by the term $eE_z^{ext}z$. This simplified representation overlooks local effects and polarization. Consequently, we observed a more pronounced control over the charge in the vdW qubit's orbitals at lower field strengths, diverging from the conclusions drawn from previous DFT analyses. To incorporate polarizability effects, we consider the static dielectric constant and define the resulting field as $E_{res} = E_z^{ext}/\epsilon_{z,hetero}$, where $\epsilon_{z,hetero}$ is the transverse dielectric permittivity of the heterostructure, accounting for any induced field present in the system. To compute $\epsilon_{z,hetero}$, we individually considered the dielectric constants of the layers constituting the heterostructure, following a similar reasoning to the quantum electrostatic heterostructure model, that
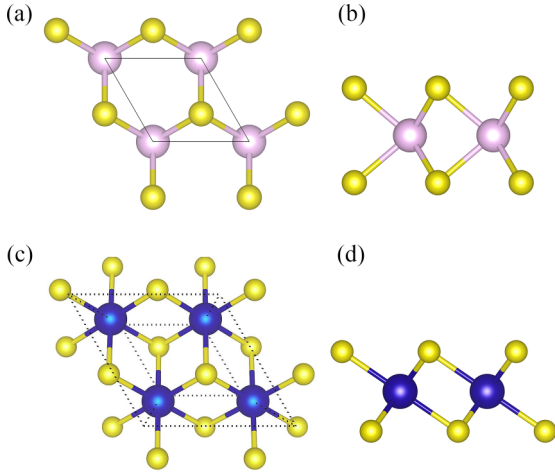
FIG. 1. 1×1 unit cell of layered materials investigated. (a) Top and (b) side view of allotrope H. (c) Top and (d) side view of allotrope T.

determines the heterostructure's dielectric function by considering the electrostatic interactions among its components [70]. Here, we approximate the heterostructure's dielectric constant as the harmonic mean of these individual constants, in which the resultant dielectric constant is given by

$$\epsilon_{z,\text{hetero}} = \frac{\epsilon_1\epsilon_2(d_1 + d_2)}{\epsilon_1 d_2 + \epsilon_2 d_1}, \tag{8}$$

where $\epsilon_{1,2}$ is the 2D dielectric constant of the layers that composes the material and $d_{1,2}$ is their thickness. Since TMDs layers possess similar thickness, we can approximate $d_1 \approx d_2$, giving

$$\epsilon_{z,\text{hetero}} \approx \frac{2\epsilon_1\epsilon_2}{\epsilon_1 + \epsilon_2}. \tag{9}$$

In this way, polarizability effects can be considered allowing the use of the model for large-scale simulations of realistic devices.

All the dielectric constants used in this work were taken from the Materials Project Database [71,72] which were computed within density functional perturbation theory approach [73,74].

III. RESULTS AND DISCUSSION

A. Structural properties

TMDs are compounds with the form X-M-X, where X is a chalcogen and M is a metal connected by covalent bonds and displaying hexagonal symmetry. Two typical structural phases are the 2H (trigonal prismatic) and 1T (octahedral) phases, which belong to the D_{3h} and D_{3d} point groups, respectively. The 2H phase has chalcogen atoms located on top of each other in the perpendicular direction of the layer. In contrast, the 1T phase has the chalcogen atoms rotated by an angle of 180° relative to the metal. Top and side view is shown of each allotrope is shown on Fig. 1.

The present work investigate the structural and electronic properties of 20 phases of 10 TMDs to obtain the necessary data for forming heterostructures and analyzing their energy

TABLE II. Structural parameters, lattice constants a (obtained in this study) and a_{exp} (derived from experimental data), and metal-chalcogen bond lengths (d_{MX}). Values in parentheses represent literature-derived data for comparison purposes.

	a (Å)	a_{exp} (Å)	d_{MX} (Å)
HfS$_2^*$(T)	3.649	3.635 [75]	2.56 (2.55 [76])
HfS$_2$ (H)	3.540	3.37 [77]	2.58
HfSe$_2^*$(T)	3.774	3.748 [75]	2.69 (2.67 [76])
HfSe$_2$ (H)	3.68	3.44 [77]	2.71
MoS$_2$ (T)	3.19	3.16 [78]	2.43
MoS$_2^*$(H)	3.185	3.162 [75]	2.41 (2.41 [79])
MoSe$_2$ (T)	3.29		2.56
MoSe$_2^*$(H)	3.322	3.289 [75]	2.54 (2.54 [79])
SnS$_2^*$(T)	3.705	3.648 [80]	2.60 (2.59 [76])
SnS$_2$ (H)	3.62	3.647 [81]	2.64
SnSe$_2^*$(T)	3.872	3.811 [80]	2.75 (2.73 [76])
SnSe$_2$ (H)	3.80	3.811 [81]	2.79
WS$_2$ (T)	3.21		2.43
WS$_2^*$(H)	3.187	3.153 [75]	2.42 (2.42 [79])
WSe$_2$ (T)	3.29		2.57
WSe$_2^*$(H)	3.321	3.282 [75]	2.55 (2.55 [79])
ZrS$_2^*$(T)	3.685	3.662 [75]	2.57 (2.57 [79])
ZrS$_2$ (H)	3.57		2.59
ZrSe$_2^*$(T)	3.750	3.700 [75]	2.70 (2.71 [79])
ZrSe$_2$ (H)	3.71		2.73

alignments. The lattice parameters (a) and the bond length between metal (M) and chalcogen (X) (d_{MX}) for each of the 2D materials are provided in Table II.

Phase engineering methods have enabled the experimental growth of TMDs that are not achievable through conventional procedures. For instance, MoS$_2$ can be synthesized in its 1T phase via ion intercalation techniques, where a significant charge transfer from ions triggers the phase transition to octahedral [82]. Similarly, substitutional doping of rhenium in WS$_2$ nanotubes results in the 1T phase, with the Re impurity atoms acting as electron donors [83]. Lithium insertion has been shown to induce the formation of 1T MoS$_2$ and WS$_2$ [84]. Combining ball milling and chemical lithium intercalation yields high percentages of 1T WS$_2$ and MoSe$_2$ from their 2H phase, producing in single-layer TMD nanodots [85]. Likewise, different growing conditions have been shown to lead to the formation of 2H phases of SnS$_2$ and SnSe$_2$ [81]. First-principles calculations also allow the simulation of phase transitions under diverse conditions, guiding experimental routes. For example, hydrogenation can induce a phase transition (H to T and vice versa) for HfS$_2$, HfSe$_2$, WSe$_2$, ZrS$_2$, and ZrSe$_2$, resulting in the interplay between metallic and semiconductor behavior depending on the layer's side exposed to the process [86]. Layered 1H SnS$_2$ can be obtained by *in situ* heating and electron beam radiation, with the growth of each phase being controllable by adjusting experimental parameters [87]. Similarly, 2H SnSe$_2$ can be assembled using the Bridgman-grown method [88].

Our *ab initio* findings, as presented in Table II, emphasize the remarkable accuracy of our results, even for less common allotropes, when compared to experimental data. The deviations from experimental values in lattice parameters and

TABLE III. Electronic properties of monolayers TMDs. Quasi-particle band gaps (E_g), ionization energies (I), and electron affinity (A) with respect to the vacuum level obtained with hybrid exchange-correlation functional HSE06.

	E_g (eV)	I (eV)	A (eV)
HfS$_2^*$(T)	2.19	7.08	4.89
HfS$_2$ (H)	1.97	7.67	5.70
HfSe$_2^*$(T)	1.53	6.37	4.84
HfSe$_2$ (H)	1.74	7.19	5.45
MoS$_2$ (T)	Metal	Metal	Metal
MoS$_2^*$(H)	2.35	6.45	4.10
MoSe$_2$ (T)	Metal	Metal	Metal
MoSe$_2^*$(H)	1.89	5.89	4.00
SnS$_2^*$(T)	2.25	7.40	5.15
SnS$_2$ (H)	1.39	6.96	5.57
SnSe$_2^*$(T)	1.41	6.72	5.31
SnSe$_2$ (H)	0.58	6.28	5.70
WS$_2$ (T)	Metal	Metal	Metal
WS$_2^*$(H)	2.49	6.20	3.71
WSe$_2$ (T)	Metal	Metal	Metal
WSe$_2^*$(H)	2.03	5.63	3.60
ZrS$_2^*$(T)	2.07	7.11	5.04
ZrS$_2$ (H)	1.81	7.58	5.77
ZrSe$_2^*$(T)	1.30	6.39	5.09
ZrSe$_2$ (H)	1.61	7.13	5.52

metal-chalcogen distances were consistently within 1% or less across all allotropes.

B. Electronic properties of monolayer systems

Going beyond the structural properties, the electronic properties of the previous monolayers are investigated, including band structures, band gaps, and energy levels with respect to the vacuum level. For the electronic properties we take the quasiparticle corrections into account by applying an XC hybrid functional HSE06 to compute the electronic band states. We do not consider spin-orbit coupling (SOC) in this study. As reported in Ref. [70], the bands' splitting in the 1T phase is inhibited. While this does not apply to the 2H phase, our analysis exclusively focuses on the 1T phases of TMDs in the

context of the heterostructures, as elaborated in the following section. The valence band maximum (VBM) and conduction band minimum (CBM) were determined with respect to the vacuum level as the reference. Consequently, the ionization energy (I) is associated with VBM, expressed as VBM $= -I$, and the electron affinity (A) is associated with CBM, expressed as CBM $= -A$. Table III provides the values for I, A, and the quasiparticle energy gap E_g (where $E_g = I - A$). Figure 2 displays a more didactic view of the energy levels with respect to the vacuum level.

The values of ionization energy I and A will be important when combining individual layers because the degree of alignment of these energies will indicate the degree of hybridization between the layers.

Another critical quantity defined here is the natural band offset between the layers. This quantity is obtained as the difference between the values of I and A in the following way:

$$\Delta E_v = I(1) - I(2),$$
$$\Delta E_c = A(2) - A(1), \tag{10}$$

where ΔE_v (ΔE_c) is the valence (conduction) band offset and the indices 1 (2) represent the layers that compose the heterojunction.

The significance of quasiparticle corrections on the band structure of materials cannot be overstated. DFT calculations often underestimate the band gap, leading to inaccuracies in energy levels. Consequently, materials that demonstrate energy level alignment when quasiparticle effects are taken into account may not exhibit this characteristic in a pure DFT calculation alone.

IV. VDW HETEROSTRUCTURES

In this section, using the data of Tables II and III, we aim to discuss heterostructures that will be useful for the vdW qubits. To this end, we want materials that will have a high degree of hybridization in the VBM and CBM. To predict this, we use the band offsets ΔE_v and ΔE_c. These offsets are essential in determining the electric field's strength necessary to modulate the degree of state hybridization within the heterostructure. Given an interlayer distance denoted as d, as depicted in
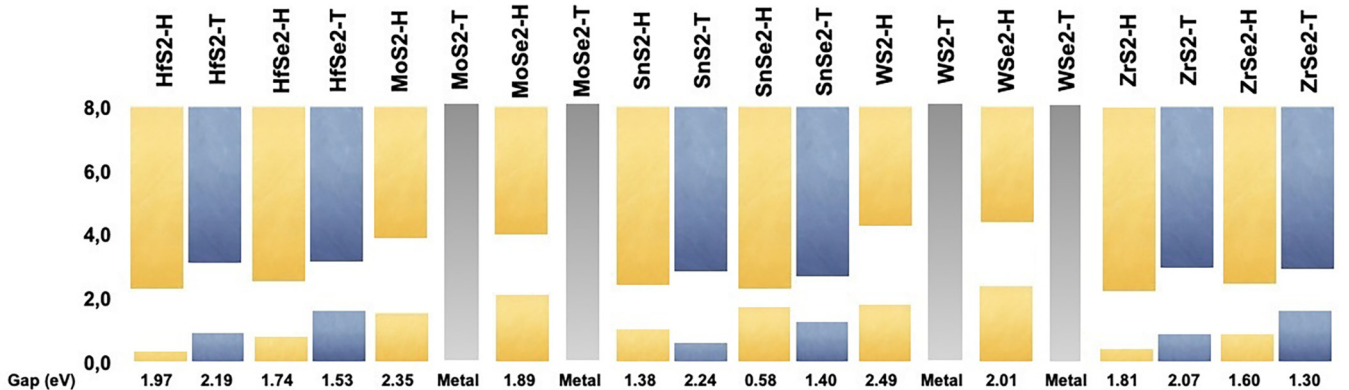

FIG. 2. Energy levels and band gaps of TMDs monolayers considering quasiparticle effects through HSE. The bar edges represent the valence band maximum and the conduction band minimum for each material. All energies are in eV and with the vacuum as reference.
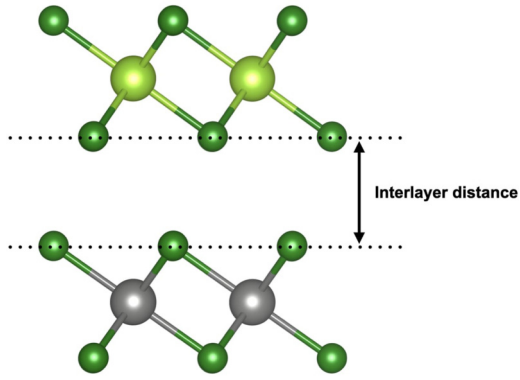
FIG. 3. An illustration of the system under investigation in this study is provided, showing a side view of the heterostructure, which consists of the 1T phase of each constituent material. Notably, the interlayer distance is visualized as it plays an important quantity in estimating the gate potential needed to modulate the hybridization within the band structure based on the band off-sets. Light green is the thin (Sn) atoms, dark green selenium (Se), and gray zirconium (Zr) atoms.

TABLE IV. Valence (ΔE_v) and (ΔE_c) conduction band offsets for the heterostructures with the pair offset lower than 0.6 eV that will be studied in detail in the following subsections. All values are in eV.

Heterostructure	I	A	ΔE_v	ΔE_c
$ZrSe_2/SnSe_2$	6.52	5.28	−0.33	0.23
HfS_2/SnS_2	7.18	5.14	−0.32	0.26
ZrS_2/SnS_2	7.17	5.26	−0.29	0.11
ZrS_2/HfS_2	7.07	5.16	0.03	−0.15

Fig. 3, the electric field is given by $E = V/d$, with V being the gate potential.

Materials pairs with offsets of less than 0.6 eV emerge as strong candidates for hosting vdW qubits through heterostructure assembly. Our investigation resulted in 222 possible combinations attending this criterion, as presented in the Supplemental Material (SM) [89]. Given an interlayer distance of approximately 3 Å, the electric field necessary to manipulate this hybridization has values around 0.2 V/Å, which is well within the applicable range for the systems investigated in this study.

Expanding on a previously proposed class of host materials [27], we broaden this classification, offering additional experimental pathways to attain platforms suitable for vdW qubits. This extension holds significance for industrial applications, aiding in the selection of economically feasible, easily accessible, and environmentally friendly materials for assembly. The new material combinations are detailed in the SM [89]. Here we delve into a subset of these combinations: $ZrSe_2/SnSe_2$, HfS_2/SnS_2, ZrS_2/SnS_2, and ZrS_2/HfS_2. Following we explore each case separately. The bottom and top layers are denoted, respectively, by BL and TL.

A. $ZrSe_2/SnSe_2$ heterostructure

To evaluate the methodology proposed in this study, we compared our results with those from a previous investigation on the $ZrSe_2/SnSe_2$ heterojunction [27]. Our investigation aimed to determine whether perturbing the onsite energies in the TB model with an electric field could achieve the same degree of hybridization control as in DFT calculations. The heterostructure, which includes stacking different layers of TMDs on top of each other, is depicted in Fig. 3. Additionally, we provide the interlayer distance for reference.

Once dealing with heterostructures, an important point to be discussed is which stacking will be considered on the *ab initio* simulations. The stacking configuration is determinant since influences not only the total energy but also crucial

quantities such as exfoliation and binding energies and the overall stability of the heterostructure. However, the stacking pattern has a negligible effect on the orbital contribution of the bands [90,91].

Concerning the structural properties, the isolated layers present a good lattice match with $ZrSe_2$ having a lattice parameter of 3.80 Å and $SnSe_2$ of 3.87 Å. When combining these materials in a heterostructure, a minor stress is applied on the monolayers to make the system commensurable, tensile on $ZrSe_2$ and compressive on $SnSe_2$. This results in a heterostructure with a lattice constant of 3.83 Å which corresponds to a relative stress of 0.9% on each layer. After the relaxation procedure, the interlayer distance resulted in 3.04 Å. Table IV presents the electronic properties of $ZrSe_2$ (BL) and $SnSe_2$ (TL). By examining the energy levels depicted in Fig. 2, we observe that these two materials exhibit a type II band alignment. The slight offsets of the layers hint at a possible hybridization presented in the band structure of the heterojunction.

To simplify the model and investigate whether the same hybridization control occurs on the two lowest conduction bands, we performed Wannierization to obtain an *ab initio* TBH from the Bloch wave functions. Based on a projected band-structure analysis, we took into account the d_{xy}, d_{z^2}, and $d_{x^2-y^2}$ orbitals of zirconium and p orbitals of selenium, resulting in a TB model consisting of 15 bands. Tin gives a minor contribution to the bands around the Fermi energy in this heterostructure and on the ones discussed in Secs. IV B and IV C and, for this reason, it was not considered in our model. However, to obtain a simplified Hamiltonian that captures the central physics of bands of interest, it is considered hoppings with magnitude above a certain threshold, here represented by |hop|, and between orbitals separated by a certain distance, d_{hop}. The values chosen to truncate the Hamiltonian while preserving the band gap and ensuring agreement of TB and DFT band structures, as well as maintaining the orbital contribution of the layers, were |hop| $\geqslant 0.024$ eV and $d_{hop} \leqslant 8.4$ Å. The resulting band structure is shown in Fig. 4. The orbital characters of the truncated Hamiltonian are 45% ($ZrSe_2$) and 55% for ($SnSe_2$) in the lowest conduction band, in good agreement with DFT results [92]. The resulting *ab initio* TBH is 1.26 eV, which is comparable with the DFT + HSE value of 1.24 eV.

If the electric field is introduced as a first-order perturbation on the onsite energies, without considering polarizability effects, then the control of the orbital character is achieved. This is illustrated in Fig. 5, where the change in hybridization can be observed. For negative fields, $|0\rangle$ comprises states
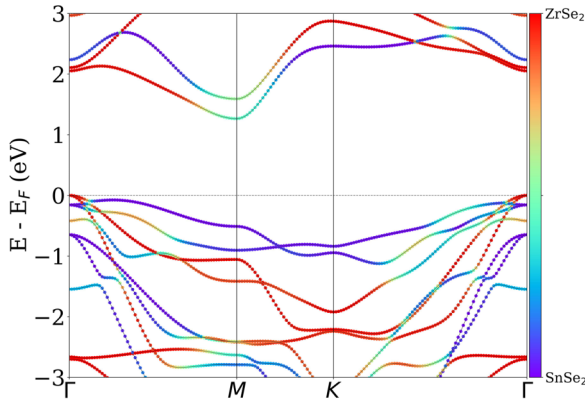
FIG. 4. Band structure of $ZrSe_2/SnSe_2$ obtained by the *ab initio* TBH. The zero of energy is considered on the top of the valence bands.

coming from $SnSe_2$, and $|1\rangle$ from $ZrSe_2$, and the opposite occurs for positive fields. Here the vdW qubit state $|\psi\rangle = \alpha|0\rangle + \beta|1\rangle$ is interpreted as being the two lowest conduction bands at the M point each having the orbital weight (α and β) which is a function of the electric field applied.

This result aligns qualitatively with the previous work that analyzed these properties from *ab initio* calculation [27]. However, due to the approximation of adding the electric field as a first-order perturbation to the onsite energies, with the hoppings held constant and given the selection of relevant orbitals for model construction, the magnitude of the electric field does not match. In the *ab initio* calculation, the electric field required to concentrate 80% of the charge in one of the layers is around -0.3 V/Å while in the TB model this is achieved at -0.04 V/Å which is one order of magnitude smaller. Moreover, although the curves of orbital control from both approaches are similar, the localization of the electronic states in the TB model is achieved with a smaller electric field.

In order to improve the quantitative results, both polarizability and local field effects are considered, taking into account the static dielectric constant. For the individual com-
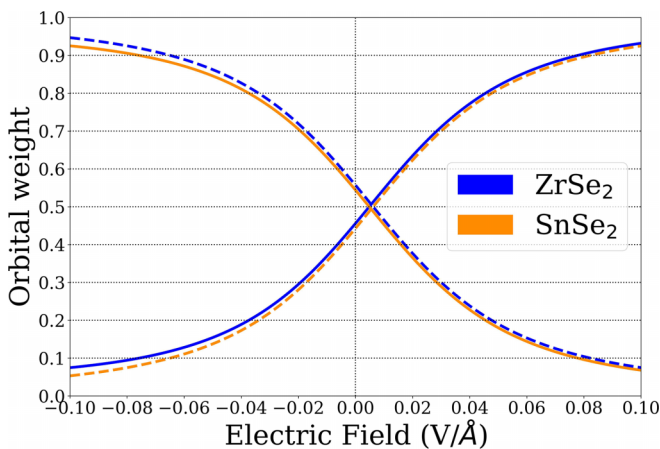
FIG. 5. Change of the orbital weight resulted from *ab initio* TB contribution as the function of the electric field applied. The solid lines represent the change on $|0\rangle$, and the dotted lines represent the change on $|1\rangle$. Blue is for $ZrSe_2$ and orange for $SnSe_2$.
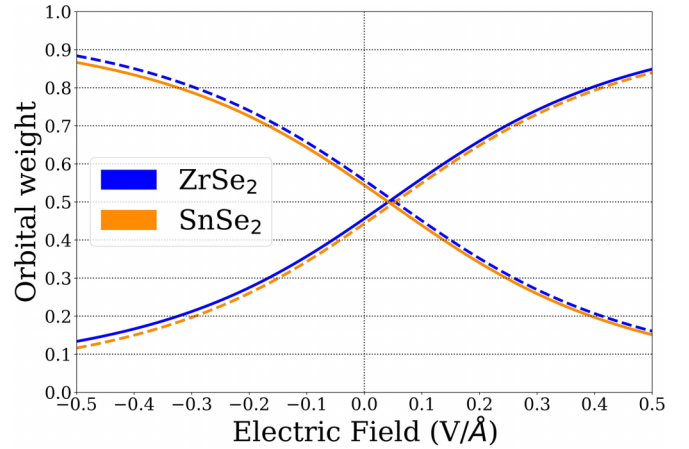

FIG. 6. The *ab initio* TBH results for the orbital contribution as a function of the electric field applied considering the effect of polarizability. The solid lines represent the change on $|0\rangle$, and the dotted lines represent the change on $|1\rangle$. Blue is for $ZrSe_2$ and orange for $SnSe_2$.

ponents, the values for the static dielectric constants are 5.81 for $ZrSe_2$ and 16.95 for $SnSe_2$. Using Eq. (9), the dielectric constant for the heterostructure is determined to be 8.65. With this adjustment, the range of fields required to manipulate the orbital composition of the two lowest conduction bands is comparable with that obtained from the DFT calculation, as illustrated in Fig. 6. In this scenario, the electric field intensity required to concentrate the orbital contribution of 80% coming from one layer is -0.32 V/Å now in agreement with the full DFT calculation.

The band structure subjected to different fields is shown in Fig. 7. Changes in the orbital composition on the two lowest conduction bands are evident as the intensity and direction of the electric field is applied. One may also note the change of orbital contribution on the valence bands at Γ point. The hole states are concentrated at the $ZrSe_2$ layer from zero towards negative fields. For positive fields, the energy levels in the valence are shifted, making the hole states concentrated in the $SnSe_2$ layer.

B. HfS_2/SnS_2 heterostructure

The HfS_2/SnS_2 heterostructure was selected for in-depth investigation, consisting of two layers on 1T phase, with six atoms in the unit cell. Despite the minor lattice mismatch between the layers, with HfS_2 layer having a lattice parameter of 3.65 Å and the SnS_2 layer 3.71 Å, an average lattice parameter was determined to establish the unit cell. This resulted in a value of 3.68 Å, with each layer experiencing a relative strain of approximately 0.8%. After the relaxation of the atomic positions in the unit cell, the interlayer distance was found to be 2.99 Å.

The heterostructure's components have already been assembled experimentally, as reported in the literature [93,94], and their potential applications have been explored. These experimental pieces of evidence make the construction of such heterostructure viable. Moreover, our *ab initio* calculations demonstrate that this stacking configuration is energetically
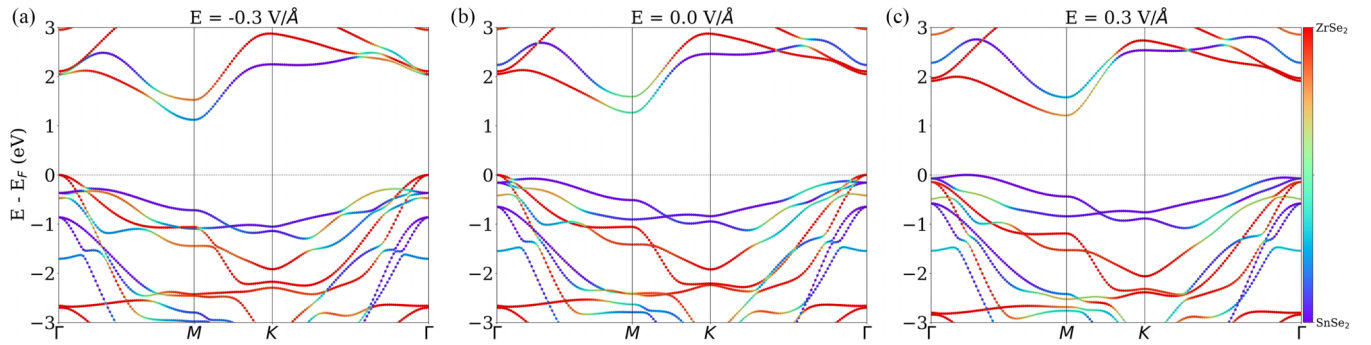
FIG. 7. Band structures for the $ZrSe_2/SnSe_2$ heterobilayer when an electric field of (a) -0.3 V/Å, (b) 0.0 V/Å, and (c) $+0.3$ V/Å is applied in the z direction. Palette color indicates the percentage of bands formed by orbitals from the $SnSe_2$ and $ZrSe_2$ layers. The top of the valence band is taken as reference.

favorable. As inferred from the previously computed energy levels, their small band offsets suggest a potential for states hybridization, possibly leading to a vdW qubit, as presented in Table IV.

From the projected band analysis of the present heterostructure, the d_{xy}, d_{z^2}, and $d_{x^2-y^2}$ orbitals of hafnium and p orbitals of sulfur were identified as significant contributors to the low-energy bands. Consequently, these orbitals were used as an initial guess for the Wannierizartion procedure to obtain the MLWFs. This led to a TB model of 15 bands. Following a similar procedure to obtain the parameters to truncate the sparse Hamiltonian ensuring the preservation of the main quantities of interest, the values were set a $d_{hop} \leqslant 7$ Å and $|hop| \geqslant 0.02$ eV. This resulted in a match of DFT and TB bands, where it is included hoppings up to second-neighbor interactions. The resulted *ab initio* TBH band gap is 2.0 eV, in good agreement with the DFT + HSE06 value of 2.04 eV. Furthermore, the orbital contribution of the HfS_2 (SnS_2) for the lowest conduction band is 64% (36%) at the M point, which has also an excellent agreement with previous DFT results [92]. Proceeding with the approximation of inserting the electric field on the onsite energies, the magnitude of the electric field applied is similar to the previous case of the $ZrSe_2/SnSe_2$ system. The band structures are shown in Fig. 8.

Following the same notation as for the previous system, the orbital character change with the applied electric field is given in Fig. 9 where the polarizability effects were already taken into account. The dielectric constant of the heterostructure is 4.97.

C. ZrS_2/SnS_2 heterostructure

Based on the previous two systems, it is verified that the ability to control the orbital character is not unique to a particular vdW heterostructure but rather a general phenomenon. The alignment of energy levels in the individual layers prior to their combination in a heterostructure serves as a useful parameter for guiding the design of vdW qubits. This approach can be applied to various host materials, which makes vdW qubits attractive for electronic component applications due to the abundance of vdW materials available experimentally.

Similarly to the previous heterostructure discussed in this section, here only the chalcogen is replaced, Se to S, yielding on the ZrS_2/SnS_2 heterostructure, where both materials are also in their 1T phase. A 1×1 unit cell is also suitable for this system due to the minor mismatch between of ZrS_2 (3.69 Å) and SnS_2 (3.71 Å). Averaging these values gives a lattice parameter of 3.70 Å inducing a relative stress of roughly 0.3% on each layer. Postcomplete relaxation, the interlayer distance measured at 2.95 Å.

Concerning the electronic properties, this heterostructure also exhibits a small offset in the conduction bands, which can be useful for a host material for the vdW qubit. The energy levels involved in this system are summarized in Table IV.
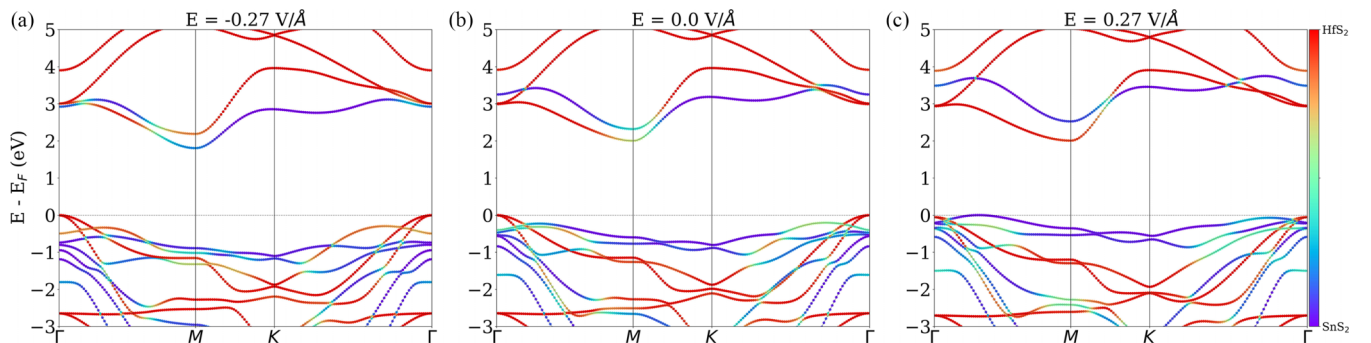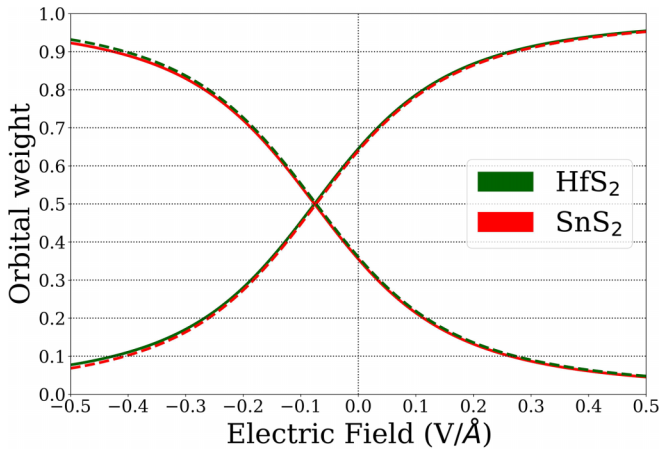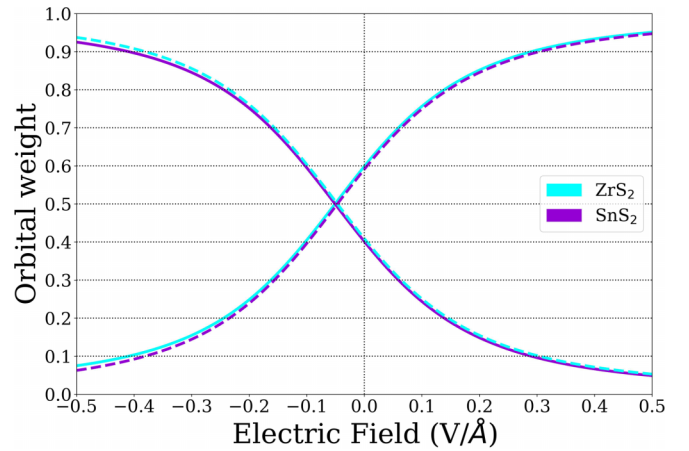

FIG. 8. Band structures for the HfS_2/SnS_2 heterobilayer when an electric field of (a) -0.27 V/Å, (b) 0.0 V/Å, and (c) $+0.27$ V/Å is applied in the z direction. Palette color indicates the percentage of bands formed by orbitals from the HfS_2 and SnS_2 layers. The top of the valence band is taken as reference.

FIG. 9. Same as Fig. 6 but now for HfS_2/SnS_2.

FIG. 11. The same of Fig. 6 but now for ZrS_2/SnS_2.

The band structure of this system is similar to that of $ZrSe_2/SnSe_2$, which is expected since the chalcogen atoms in both systems belong to the same family on the periodic table and the calculated band gap, considering quasiparticle effects, was 1.91 eV. The TB model derived from Wannierization used the same atomic orbitals as in the previous systems, given the similar chemistry of the compounds. The TB model featured 15 bands and a band gap of 1.89 eV, a value that closely matches the *ab initio* result of 1.91 eV. The TB Hamiltonian was truncated considering $d_{hop} \leqslant 8.5$ Å and $|hop| \geqslant 0.004$ eV where, besides first- and second- neighbor, 10 third-neighbor hoppings were included to improve the agreement of the orbital character between DFT and the TB model.

The resulting band structure for this gated system is shown in Fig. 10. Similarly to the case of the heterostructure $ZrSe_2/SnSe_2$, for negative fields the state $|0\rangle$ is mainly composed of state coming from the SnS_2 layer and $|1\rangle$ from ZrS_2 layer and the modulation of this contribution changes with the intensity and direction of the electric field. A similar change in the orbital composition is also observed at the top of the valence band. The dielectric constant for this heterostructure is 5.48.

The orbital control, shown in Fig. 11, indicates that with a field around -0.24 V/Å it is possible to concentrate 80% of the charge coming from one of the layers to each qubit state, a value that is in agreement with the two other systems

investigated. Around 0.14 V/Å is required for positive fields to localize the qubit state in one of the layers.

D. ZrS_2/HfS_2 heterostructure

Up to this point, we have been discussing systems with a small band offset in the conduction bands. However, we will now examine a system that exhibits the superposition of states not in conduction but rather in the valence bands. Specifically, we consider the ZrS_2/HfS_2 heterostructure, consisting of both materials in the 1T phase and six atoms in the unit cell. In this case, the lattice parameters of the individual layers are nearly commensurate, allowing for a 1×1 unit cell. At the commensurate lattice constant, each layer is subjected to a relative strain of only 0.5%, and the interlayer distance where the energy is minimized is 2.98 Å.

As seen in Table IV, the valence band offset is $\Delta E_v = 0.03$ eV, indicating that the energy levels of the individual layers are nearly aligned, suggesting a strong hybridization between these states. The CBM of the individual layers also exhibits a small offset of $\Delta E_c = -0.15$ eV.

To confirm this observation, we conducted a Wannierization analysis using the d_{xy}, d_{z^2}, and $d_{x^2-y^2}$ orbitals of zirconium and hafnium, as well as the p orbitals of sulfur, which were identified through a fat band analysis. This resulted in a basis of 18 atomic orbitals that were minimized
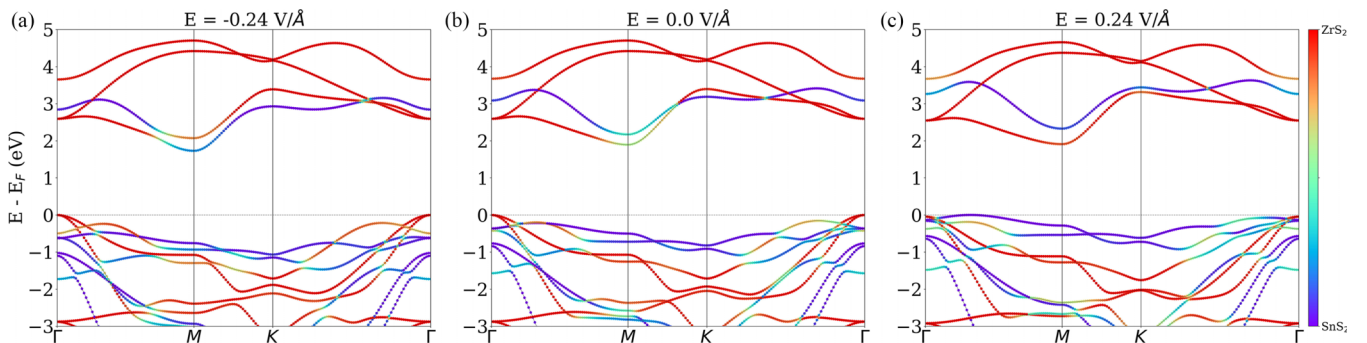

FIG. 10. Band structures for the ZrS_2/SnS_2 heterobilayer when an electric field of (a) -0.24 V/Å, (b) 0.0 V/Å, and (c) $+0.24$ V/Å is applied in the z direction. Palette color indicates the percentage of bands formed by orbitals from the ZrS_2 and SnS_2 layers. The top of the valence band is taken as reference.
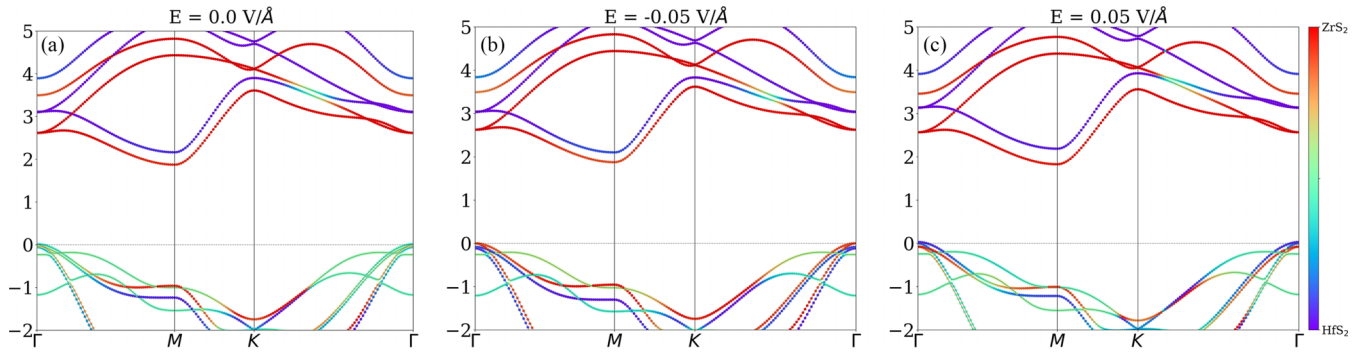
FIG. 12. Band structures for the ZrS$_2$/HfS$_2$ heterobilayer when an electric field of (a) 0.0 V/Å, (b) -0.05 V/Å, and (c) $+0.05$ V/Å is applied in the z direction showing the change of hybridization at the Γ point. Palette color indicates the percentage of bands formed by orbitals from the ZrS$_2$ and HfS$_2$ layers. The top of the valence band is taken as reference.

to produce the MLWFs. The resulting TB band structure of the vdW heterostructure is depicted in Fig. 12. As expected, the alignment of energy levels of individual layers results in hybridization on the valence bands. The band gap obtained from the DFT + HSE06 calculation was 1.90 eV, while the TB model yielded a gap of 1.86 eV. To reduce the Hamiltonian, only hoppings with a modulo |hop| $\geqslant$ 0.02 eV and between neighbors located at a distance below $d_{\text{hop}} \leqslant 8.0$ Å were kept, considering only first and second neighbors.

One can observe in Fig. 12 that in this heterostructure, having the dielectric constant of 3.75, it is possible to confine holes in one of the layers at the Γ point by applying very small electric fields ($\pm$ 0.05 V/Å). Specifically, a negative electric field leads to hole localization in the ZrS$_2$ layer, whereas a positive field leads to hole concentration in the HfS$_2$ layer.

Due to the versatility of modeling electronic properties in vdW heterostructures, hybridization can also be made to occur in the conduction bands in this system. The hybridization "jumps" from the valence bands to the two lowest conduction bands for more intense and negative electric fields, resulting in a two-level system similar to the previous heterostructures. This system demonstrates the ability to manipulate the electronic structures of vdW heterostructures, allowing for control over the superposition of quantum states in either the valence

or the conduction bands, which can affect transport properties. In this case, an electric field is used to first obtain the desired superposition of quantum states in the two lowest conduction bands, resulting in a charge distribution between the layers, or a two-level system of $|0\rangle$ and $|1\rangle$, followed by further control of the charge contribution of each layer for this qubit. Figure 13 clearly shows that as the electric field is turned on, the electron is localized in one of the layers, and the orbital character of these two bands changes.

At zero field, the state $|0\rangle$ ($|1\rangle$) is formed entirely from the ZrS$_2$ (HfS$_2$) layer and with the application of a negative electric field, this contribution changes. This change in the orbital character of the two lowest conduction bands is shown in Fig. 14

From Fig. 14, it can also be noted that the equal distribution of states for the vdW qubit is in a situation where the heterostructure is subjected to a gate field, around -0.16 V/Å, which is justified by the offset that the conduction bands presents. Since at zero field the equal contribution is on the valence, the energy levels on the conduction are aligned for negative fields, which explains the result.

The summary of the electric field required to concentrate 80% of the orbital contribution of the qubit's states is shown in Table V. It can be seen that for each system, there is a range of fields required for such manipulation of the states.
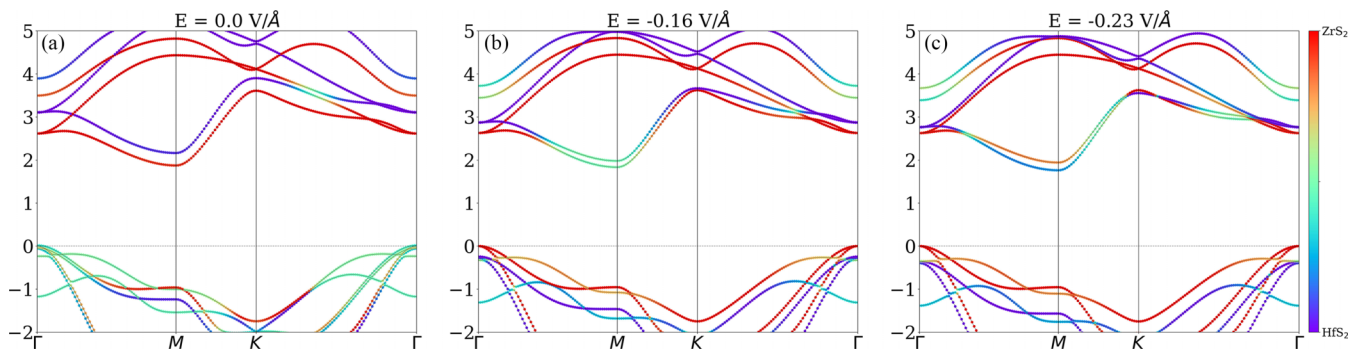

FIG. 13. Band structures for the ZrS$_2$/HfS$_2$ heterobilayer when an electric field of (a) 0.0 V/Å, (b) -0.16 V/Å, and (c) -0.23 V/Å is applied in the z direction showing the change of hybridization now at the conduction bands at the M point. Palette color indicates the percentage of bands formed by orbitals from the ZrS$_2$ and HfS$_2$ layers. The top of the valence band is taken as reference.
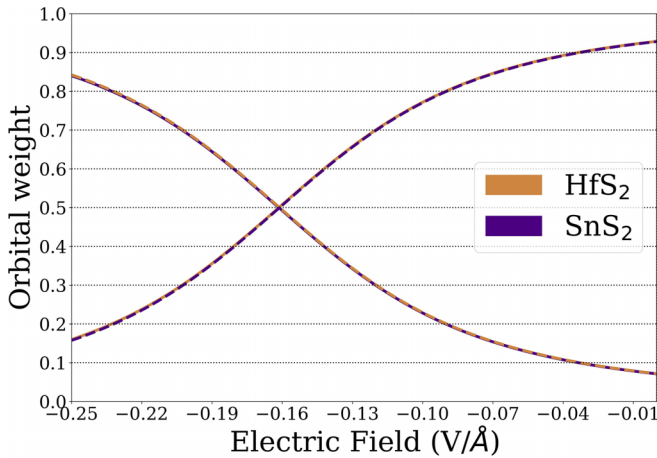
FIG. 14. The same of Fig. 9, but now for ZrS_2/HfS_2.

The smaller range of electric field required for such manipulation can be more practical once the rotations in the Bloch sphere are achieved at a smaller field. Moreover, the ZrS_2/HfS_2 system has the advantage of a field in a fixed polarization, changing only its intensity.

V. CONCLUSION

In this study, we leverage the accuracy of DFT calculations, which include quasiparticle effects, to obtain TBH for vdW heterostructures composed of monolayers of TMDs by the Wannierization method [61,62]. We investigate the structural and electronic properties of 20 TMD monolayers and combine them to form heterostructures suitable for hosting vdW qubits.

The accuracy of the *ab initio* TB model was confirmed through a comparison with a previous pure DFT calculation of the $ZrSe_2/SnSe_2$ heterostructure [27]. The findings revealed an excellent agreement for the unbiased and biased band structure. Subsequent investigations of other systems revealed a consistent tendency towards a slight energy level mismatch, leading to the emergence of hybridized states within the band structure, which could be effectively modulated by the application of a gate field. This widespread behavior across different systems suggests the potential suitability of these materials as host components for vdW qubits.

It was further confirmed that it is feasible to engineer the location of hybridization, as evidenced in the case of ZrS_2/HfS_2, where a minor offset on the valence band resulted

TABLE V. Summary of electric field required to concentrate 80% and 20% of the orbital contribution in the two lowest conduction bands.

Heterostructure	$E_{80/20}$ (V/Å)	$E_{20/80}$ (V/Å)
$ZrSe_2/SnSe_2$	−0.32	+0.30
HfS_2/SnS_2	−0.27	+0.11
ZrS_2/SnS_2	−0.24	+0.14
ZrS_2/HfS_2	−0.24	−0.09

in well-localized states in the conduction bands. However, this hybridization can be obtained in the conduction bands once an electric field is applied, obtaining the desired two-level system for the development of the vdW qubit.

The control of the orbital character of the hybridized states in the TB model occurs within the same range of fields from the *ab initio* calculations. In addition, using the 1T phase of allotropes the effect of band splitting due to SOC can be ignored, making the initial calculations less expensive.

In summary, our research has identified promising new combinations of layered materials suitable for hosting vdW qubits, offering novel possibilities for physically implementing them. Using an *ab initio* TBH, free of any external parameter, it is shown that it is possible to obtain the same accuracy of DFT for band-structure calculations but with a substantially lower computational cost. This approach opens new perspectives for simulating transport in large-scale devices such as the proposed vdW qubits.

APPENDIX: CAPABILITIES OF THE *AB INITIO* TIGHT-BINDING HAMILTONIANS

To illustrate the practical utility of *ab initio* TB models in simulating large-scale systems, we present a prototype
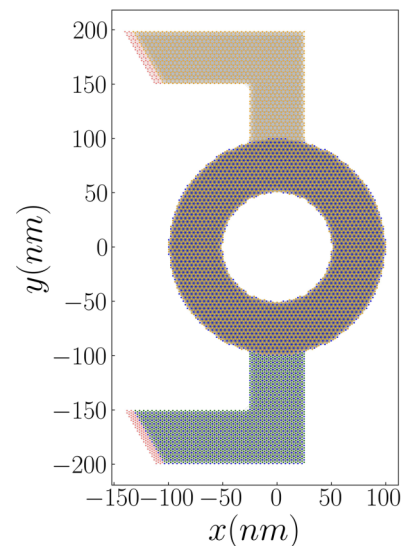

FIG. 15. Prototype device designed for studying the transport properties of highly hybridized states with 13.114 atoms.
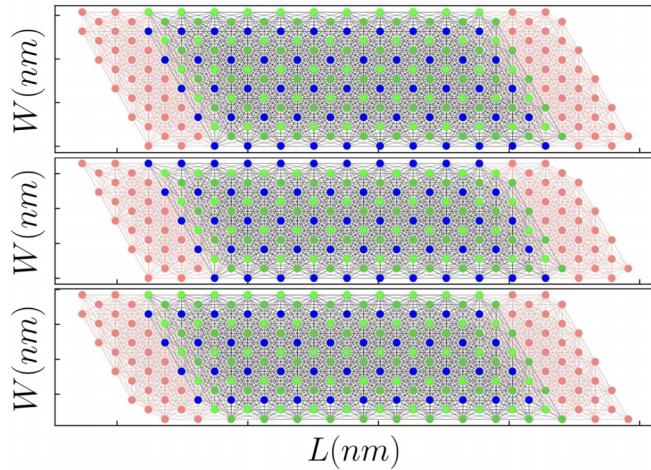
FIG. 16. Top view of ZrSe$_2$ NR with different edge termination. From top to bottom: metal-chalcogen (MC), metal-metal (MM) and chalcogen-chalcogen (CC) edges.

FIG. 17. Conductance (G) as a function of energy (E) for ZrSe$_2$ NRs with metal-chalcogen (MC), metal-metal (MM), and chalcogen-chalcogen (CC) edges. The conductance for a scattering region with a circular geometry is represented by the black curve, highlighting its distinct impact on conductance. Inset: A zoomed view of the conductance near the threshold energy region, illustrating detailed behavior for energies between 1.20 and 1.40 eV.

device designed for studying the transport properties of highly hybridized states, depicted in Fig. 15. This demonstration underscores the efficacy of such models in exploring complex electronic phenomena within mesoscale structures.

The prototype comprises upper (lower) arms composed of ZrSe$_2$ (SnSe$_2$) nanoribbons and a circular central scattering region constructed based on the TB parameters defining the ZrSe$_2$/SnSe$_2$ heterostructure. This configuration encompasses 13.114 atoms and the numerical calculations can be performed without much computational effort. Notably, the TB parameters can be seamlessly integrated into KWANT software [95]. Electric and magnetic fields can be easily introduced if desired.

Furthermore, the simulations are not limited to static perturbations over time; rather, they can be extended to encompass time-dependent quantum dynamics of mesoscopic
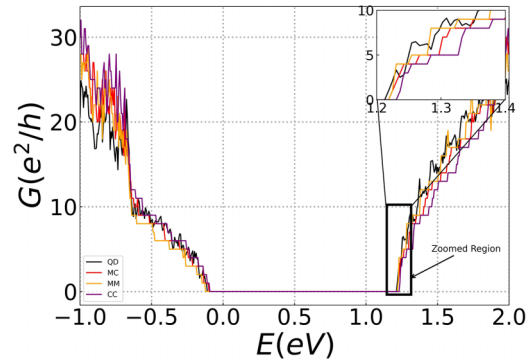
systems effortlessly, even within structures of this scale. This capability is facilitated by the TKWANT software [96], which enables the simulation of dynamic phenomena in systems with a similar order of atoms.

We can also explore simpler systems, such as nanoribbons (NRs) based on these TMDs, with different edge terminations as shown in Fig. 16. Edge states naturally emerge with the confinement of 2D materials in one more dimension, obtaining the NRs. For each edge, we have subtleties on the conductance and its quantization, as can be seen from Fig. 17.

We find that the TB models obtained in this study possess the capacity to surpass the limitations of DFT calculations for systems of this magnitude. The parameters provided in the SM lay the groundwork for exploring mesoscopic systems utilizing data derived from *ab initio* computations.

---

[1] R. Feynman, Simulating physics with computers, Int. J. Theor. Phys. **21**, 467 (1982).

[2] D. Deutsch and R. Penrose, Quantum theory, the church-turing principle and the universal quantum computer, Proc. Roy. Soc. Lond. A **400**, 97 (1985).

[3] S. Sadana, L. Maccone, and U. Sinha, Testing quantum foundations with quantum computers, Phys. Rev. Res. **4**, L022001 (2022).

[4] V. Bouchiat, D. Vion, P. Joyez, D. Esteve, and M. H. Devoret, Quantum coherence with a single cooper pair, Phys. Scr. **1998**, 165 (1998).

[5] Y. Nakamura, C. D. Chen, and J. S. Tsai, Spectroscopy of energy-level splitting between two macroscopic quantum states of charge coherently superposed by Josephson coupling, Phys. Rev. Lett. **79**, 2328 (1997).

[6] Y. Nakamura, Y. Pashkin, and J. Tsai, Coherent control of macroscopic quantum states in a single-cooper-pair box, Nature (London) **398**, 786 (1999).

[7] B. Kane, A silicon-based nuclear spin quantum computer, Nature (London) **393**, 133 (1998).

[8] X. Gao, S. Vaidya, and K. Li, Nuclear spin polarization and control in hexagonal boron nitride, Nat. Mater. **21**, 1024 (2022).

[9] M. Riebe, H. Häffner, and C. Roos, Deterministic quantum teleportation with atoms, Nature (London) **429**, 734 (2004).

[10] H. Häffner, W. Hänsel, and C. Roos, Scalable multiparticle entanglement of trapped ions, Nature (London) **438**, 643 (2005).

[11] A. Gaita-Ariño, F. Luis, and S. Hill, Molecular spins for quantum computation, Nat. Chem. **11**, 301 (2019).

[12] M. R. Wasielewski, M. Forbes, and N. Frank, Exploiting chemistry and molecular systems for quantum information science, Nat. Rev. Chem. **4**, 490 (2020).

[13] C. Beenakker, Search for majorana fermions in superconductors, Annu. Rev. Condens. Matter Phys. **4**, 113 (2013).

[14] A. Chatterjee, P. Stevenson, and S. Franceschi, Semiconductor qubits in practice, Nat. Rev. Phys. **3**, 157 (2021).

[15] G. Wolfowicz, F. Heremans, and C. Anderson, Quantum guidelines for solid-state spin defects, Nat. Rev. Mater. **6**, 906 (2021).

[16] M. Toth and I. Aharonovich, Single photon sources in atomically thin materials, Annu. Rev. Phys. Chem. **70**, 123 (2019).

[17] A. L. Exarhos, D. A. Hopper, R. R. Grote, A. Alkauskas, and L. C. Bassett, Optical signatures of quantum emitters in suspended hexagonal boron nitride, ACS Nano **11**, 3328 (2017).

[18] C. Liu, H. Chen, and S. Wang, Two-dimensional materials for next-generation computing technologies, Nat. Nanotechnol. **15**, 545 (2020).

[19] A. Montblanch, M. Barbone, and I. Aharonovich, Layered materials as a platform for quantum technologies, Nat. Nanotechnol. **18**, 555 (2023).

[20] Q. Wang, K. Kalantar-Zadeh, and A. Kis, Electronics and optoelectronics of two-dimensional transition metal dichalcogenides, Nat. Nanotechnol. **7**, 699 (2012).

[21] A. Splendiani, L. Sun, Y. Zhang, T. Li, J. Kim, C.-Y. Chim, G. Galli, and F. Wang, Emerging photoluminescence in monolayer MoS_2, Nano Lett. **10**, 1271 (2010).

[22] K. S. Novoselov, A. K. Geim, S. V. Morozov, D. Jiang, Y. Zhang, S. V. Dubonos, I. V. Grigorieva, and A. A. Firsov, Electric field effect in atomically thin carbon films, Science **306**, 666 (2004).

[23] C. Lee, X. Wei, J. W. Kysar, and J. Hone, Measurement of the elastic properties and intrinsic strength of monolayer graphene, Science **321**, 385 (2008).

[24] N. Wu, X. Zhao, X. Ma, Q. Xin, X. Liu, T. Wang, and S. Wei, Strain effect on the electronic properties of 1t-HfS_2 monolayer, Phys. E **93**, 1 (2017).

[25] X. Tong, L. Fang, and R. Liu, Strain-induced electronic properties of van der waals heterostructures based on tin dichalcogenides, AIP Adv. **9**, 055324 (2019).

[26] B. Radisavljevic, A. Radenovic, and J. Brivio, Single-layer MoS_2 transistors, Nat. Nanotechnol. **6**, 147 (2011).

[27] B. Lucatto, D. S. Koda, F. Bechstedt, M. Marques, and L. K. Teles, Charge qubit in van der waals heterostructures, Phys. Rev. B **100**, 121406(R) (2019).

[28] A. Geim and I. Grigorieva, Van der waals heterostructures, Nature (London) **499**, 419 (2013).

[29] C. Gong, H. Zhang, W. Wang, L. Colombo, R. M. Wallace, and K. Cho, Band alignment of two-dimensional transition metal dichalcogenides: Application in tunnel field effect transistors, Appl. Phys. Lett. **103**, 053513 (2013).

[30] B. Amin, N. Singh, and U. Schwingenschlögl, Heterostructures of transition metal dichalcogenides, Phys. Rev. B **92**, 075439 (2015).

[31] F. A. Rasmussen and K. S. Thygesen, Computational 2d materials database: Electronic structure of transition-metal dichalcogenides and oxides, J. Phys. Chem. C **119**, 13169 (2015).

[32] G.-B. Liu, W.-Y. Shan, Y. Yao, W. Yao, and D. Xiao, Three-band tight-binding model for monolayers of group-vib transition metal dichalcogenides, Phys. Rev. B **88**, 085433 (2013).

[33] C. Schattauer, M. Todorović, and K. Ghosh, Machine learning sparse tight-binding parameters for defects, npj Comput. Mater. **8**, 116 (2022).

[34] A. N. Rudenko, S. Yuan, and M. I. Katsnelson, Toward a realistic description of multilayer black phosphorus: From *GW* approximation to large-scale tight-binding simulations, Phys. Rev. B **92**, 085419 (2015).

[35] S. Fang, R. Kuate Defo, S. N. Shirodkar, S. Lieu, G. A. Tritsaris, and E. Kaxiras, Ab initio tight-binding hamiltonian for transition metal dichalcogenides, Phys. Rev. B **92**, 205108 (2015).

[36] P. Hohenberg and W. Kohn, Inhomogeneous electron gas, Phys. Rev. **136**, B864 (1964).

[37] W. Kohn and L. J. Sham, Self-consistent equations including exchange and correlation effects, Phys. Rev. **140**, A1133 (1965).

[38] P. Giannozzi, S. Baroni, N. Bonini, M. Calandra, R. Car, C. Cavazzoni, D. Ceresoli, G. L. Chiarotti, M. Cococcioni, I. Dabo, A. D. Corso, S. de Gironcoli, S. Fabris, G. Fratesi, R. Gebauer, U. Gerstmann, C. Gougoussis, A. Kokalj, M. Lazzeri, L. Martin-Samos *et al.*, Quantum espresso: A modular and open-source software project for quantum simulations of materials, J. Phys.: Condens. Matter **21**, 395502 (2009).

[39] P. Giannozzi, O. Andreussi, T. Brumme, O. Bunau, M. B. Nardelli, M. Calandra, R. Car, C. Cavazzoni, D. Ceresoli, M. Cococcioni, N. Colonna, I. Carnimeo, A. D. Corso, S. de Gironcoli, P. Delugas, R. A. DiStasio, A. Ferretti, A. Floris, G. Fratesi, G. Fugallo *et al.*, Advanced capabilities for materials modelling with quantum espresso, J. Phys.: Condens. Matter **29**, 465901 (2017).

[40] P. Giannozzi, O. Baseggio, P. Bonfà, D. Brunato, R. Car, I. Carnimeo, C. Cavazzoni, S. de Gironcoli, P. Delugas, F. Ferrari Ruffino, A. Ferretti, N. Marzari, I. Timrov, A. Urru, and S. Baroni, Quantum espresso toward the exascale, J. Chem. Phys. **152**, 154105 (2020).

[41] H. J. Monkhorst and J. D. Pack, Special points for brillouin-zone integrations, Phys. Rev. B **13**, 5188 (1976).

[42] T. Sohier, M. Calandra, and F. Mauri, Density functional perturbation theory for gated two-dimensional heterostructures: Theoretical developments and application to flexural phonons in graphene, Phys. Rev. B **96**, 075448 (2017).

[43] D. R. Hamann, M. Schlüter, and C. Chiang, Norm-conserving pseudopotentials, Phys. Rev. Lett. **43**, 1494 (1979).

[44] D. R. Hamann, Optimized norm-conserving vanderbilt pseudopotentials, Phys. Rev. B **88**, 085117 (2013).

[45] D. R. Hamann, Erratum: Optimized norm-conserving vanderbilt pseudopotentials [Phys. Rev. B **88**, 085117 (2013)], Phys. Rev. B **95**, 239906(E) (2017).

[46] M. van Setten, M. Giantomassi, E. Bousquet, M. Verstraete, D. Hamann, X. Gonze, and G.-M. Rignanese, The pseudodojo: Training and grading a 85 element optimized norm-conserving pseudopotential table, Comput. Phys. Commun. **226**, 39 (2018).

[47] J. P. Perdew, K. Burke, and M. Ernzerhof, Generalized gradient approximation made simple, Phys. Rev. Lett. **77**, 3865 (1996).

[48] J. P. Perdew, K. Burke, and M. Ernzerhof, Generalized gradient approximation made simple [Phys. Rev. Lett. **77**, 3865 (1996)], Phys. Rev. Lett. **78**, 1396(E) (1997).

[49] J. Heyd, G. E. Scuseria, and M. Ernzerhof, Hybrid functionals based on a screened coulomb potential, J. Chem. Phys. **118**, 8207 (2003).

[50] J. Heyd, G. E. Scuseria, and M. Ernzerhof, Erratum: Hybrid functionals based on a screened coulomb potential [J. Chem. Phys. **118**, 8207 (2003)], J. Chem. Phys. **124**, 219906(E) (2006).

[51] A. V. Krukau, O. A. Vydrov, A. F. Izmaylov, and G. E. Scuseria, Influence of the exchange screening parameter on the performance of screened hybrid functionals, J. Chem. Phys. **125**, 224106 (2006).

[52] L. Lin, Adaptively compressed exchange operator, J. Chem. Theory Comput. **12**, 2242 (2016).

[53] F. Gygi and A. Baldereschi, Self-consistent hartree-fock and screened-exchange calculations in solids: Application to silicon, Phys. Rev. B **34**, 4405 (1986).

[54] K. Kunc and R. Resta, External fields in the self-consistent theory of electronic states: A new method for direct evaluation of macroscopic and microscopic dielectric response, Phys. Rev. Lett. **51**, 686 (1983).

[55] J. Tóbik and A. Dal Corso, Electric fields with ultrasoft pseudopotentials: Applications to benzene and anthracene, J. Chem. Phys. **120**, 9934 (2004).

[56] T. Thonhauser, S. Zuluaga, C. A. Arter, K. Berland, E. Schröder, and P. Hyldgaard, Spin signature of nonlocal correlation binding in metal-organic frameworks, Phys. Rev. Lett. **115**, 136402 (2015).

[57] T. Thonhauser, V. R. Cooper, S. Li, A. Puzder, P. Hyldgaard, and D. C. Langreth, Van der waals density functional: Self-consistent potential and the nature of the van der Waals bond, Phys. Rev. B **76**, 125112 (2007).

[58] D. C. Langreth, B. I. Lundqvist, S. D. Chakarova-Käck, V. R. Cooper, M. Dion, P. Hyldgaard, A. Kelkkanen, J. Kleis, L. Kong, S. Li, P. G. Moses, E. Murray, A. Puzder, H. Rydberg, E. Schröder, and T. Thonhauser, A density functional for sparse matter, J. Phys.: Condens. Matter **21**, 084203 (2009).

[59] J. Klimeš, D. R. Bowler, and A. Michaelides, Chemical accuracy for the van der Waals density functional, J. Phys.: Condens. Matter **22**, 022201 (2010).

[60] G. H. Wannier, The structure of electronic excitation levels in insulating crystals, Phys. Rev. **52**, 191 (1937).

[61] N. Marzari and D. Vanderbilt, Maximally localized generalized Wannier functions for composite energy bands, Phys. Rev. B **56**, 12847 (1997).

[62] I. Souza, N. Marzari, and D. Vanderbilt, Maximally localized Wannier functions for entangled energy bands, Phys. Rev. B **65**, 035109 (2001).

[63] A. A. Mostofi, J. R. Yates, Y.-S. Lee, I. Souza, D. Vanderbilt, and N. Marzari, wannier90: A tool for obtaining maximally-localised Wannier functions, Comput. Phys. Commun. **178**, 685 (2008).

[64] A. A. Mostofi, J. R. Yates, G. Pizzi, Y.-S. Lee, I. Souza, D. Vanderbilt, and N. Marzari, An updated version of wannier90: A tool for obtaining maximally-localised wannier functions, Comput. Phys. Commun. **185**, 2309 (2014).

[65] G. Pizzi, V. Vitale, R. Arita, S. Blügel, F. Freimuth, G. Géranton, M. Gibertini, D. Gresch, C. Johnson, T. Koretsune, J. Ibañez-Azpiroz, H. Lee, J.-M. Lihm, D. Marchand, A. Marrazzo, Y. Mokrousov, J. I. Mustafa, Y. Nohara, Y. Nomura, L. Paulatto *et al.*, Wannier90 as a community code: New features and applications, J. Phys.: Condens. Matter **32**, 165902 (2020).

[66] E. Blount, *Formalisms of Band Theory* (Academic Press, New York, 1962), pp. 305–373.

[67] A. Marrazzo, S. Beck, E. R. Margine, N. Marzari, A. A. Mostofi, J. Qiao, I. Souza, S. S. Tsirkin, J. R. Yates, and G. Pizzi, The wannier-functionssoftware ecosystem for materials simulations, arXiv:2312.10769.

[68] D. Gresch, Q. S. Wu, G. W. Winkler, R. Häuselmann, M. Troyer, and A. A. Soluyanov, Automated construction of symmetrized wannier-like tight-binding models from *ab initio* calculations, Phys. Rev. Mater. **2**, 103805 (2018).

[69] L. Andrinopoulos, N. D. M. Hine, and A. A. Mostofi, Calculating dispersion interactions using maximally localized Wannier functions, J. Chem. Phys. **135**, 154105 (2011).

[70] K. S. Thygesen, Calculating excitons, plasmons, and quasiparticles in 2D materials and van der waals heterostructures, 2D Mater. **4**, 022004 (2017).

[71] A. Jain, S. P. Ong, G. Hautier, W. Chen, W. D. Richards, S. Dacek, S. Cholia, D. Gunter, D. Skinner, G. Ceder, and K. A. Persson, Commentary: The Materials Project: A materials genome approach to accelerating materials innovation, APL Mater. **1**, 011002 (2013).

[72] S. P. Ong, W. D. Richards, A. Jain, G. Hautier, M. Kocher, S. Cholia, D. Gunter, V. L. Chevrier, K. A. Persson, and G. Ceder, Python materials genomics (pymatgen): A robust, open-source python library for materials analysis, Comput. Mater. Sci. **68**, 314 (2013).

[73] I. Petousis, W. Chen, G. Hautier, T. Graf, T. D. Schladt, K. A. Persson, and F. B. Prinz, Benchmarking density functional perturbation theory to enable high-throughput screening of materials for dielectric constant and refractive index, Phys. Rev. B **93**, 115151 (2016).

[74] I. Petousis, D. Mrdjenovich, and E. Ballouz, High-throughput screening of inorganic compounds for the discovery of novel dielectric and optical materials, Sci Data **4**, 160134 (2017).

[75] T. Björkman, Testing several recent van der waals density functionals for layered structures, J. Chem. Phys. **141**, 074708 (2014).

[76] D. S. Koda, F. Bechstedt, M. Marques, and L. K. Teles, Coincidence lattices of 2d crystals: Heterostructure predictions and applications, J. Phys. Chem. C **120**, 10895 (2016).

[77] C. M. O. Bastos, R. Besse, J. L. F. Da Silva, and G. M. Sipahi, *Ab initio* investigation of structural stability and exfoliation energies in transition metal dichalcogenides based on Ti-, V-, and mo-group elements, Phys. Rev. Mater. **3**, 044002 (2019).

[78] X. Gan, L. Y. S. Lee, K.-y. Wong, T. W. Lo, K. H. Ho, D. Y. Lei, and H. Zhao, 2H/1T phase transition of multilayer MoS_2 by electrochemical incorporation of S vacancies, ACS Appl. Energy Mater. **1**, 4754 (2018).

[79] H. L. Zhuang and R. G. Hennig, Computational search for single-layer transition-metal dichalcogenide photocatalysts, J. Phys. Chem. C **117**, 20440 (2013).

[80] O. Madelung, U. Rossler, and M. Schulz, *Non-tetrahedrally Bonded Elements and Binary Compounds* (Springer, Berlin, 1998), Vol. 41.

[81] B. Pałosz and E. Salje, Lattice parameters and spontaneous strain in AX_2 polytypes: CdI_2, PbI_2 SnS_2 and $SnSe_2$, J. Appl. Crystallogr. **22**, 622 (1989).

[82] M. A. Py and R. R. Haering, Structural destabilization induced by lithium intercalation in MoS_2 and related compounds, Can. J. Phys. **61**, 76 (1983).

[83] A. N. Enyashin, L. Yadgarov, L. Houben, I. Popov, M. Weidenbach, R. Tenne, M. Bar-Sadan, and G. Seifert, New route for stabilization of 1t-WS_2 and MoS_2 phases, J. Phys. Chem. C **115**, 24586 (2011).

[84] M. Kan, J. Y. Wang, X. W. Li, S. H. Zhang, Y. W. Li, Y. Kawazoe, Q. Sun, and P. Jena, Structures and phase transition of a MoS_2 monolayer, J. Phys. Chem. C **118**, 1515 (2014).

[85] C. Tan, Z. Luo, A. Chaturvedi, Y. Cai, Y. Du, Y. Gong, Y. Huang, Z. Lai, X. Zhang, L. Zheng, X. Qi, M. H. Goh, J. Wang, S. Han, X.-J. Wu, L. Gu, C. Kloc, and H. Zhang, Preparation

of high-percentage 1T-phase transition metal dichalcogenide nanodots for electrochemical hydrogen evolution, Adv. Mater. **30**, 1705509 (2018).

[86] Y. Qu, H. Pan, and C. Kwok, Hydrogenation-controlled phase transition on two-dimensional transition metal dichalcogenides and their unique physical and catalytic properties, Sci. Rep. **6**, 34186 (2016).

[87] R. Xie, M. Hu, D. Liu, Y. Yu, C. Li, J. He, and J. Luo, Atomic observation of phase transition in layered SnS_2 driven by in situ heating and electron beam irradiation, Appl. Phys. Lett. **117**, 163103 (2020).

[88] Y. Bertrand, F. Solal, and F. Levy, Experimental band structure of 2H-$SnSe_2$ by synchrotron radiation photoemission spectroscopy, J. Phys. C **17**, 2879 (1984).

[89] See Supplemental Material at http://link.aps.org/supplemental/10.1103/PhysRevB.109.125416 for tight-binding parameters (hopping terms and onsite energies) of the van der Waals heterostructures discussed on Sec. IV of the main manuscript.

[90] W. Ju, Y. Zhang, T. Li, D. Wang, E. Zhao, G. Hu, Y. Xu, and H. Li, A type-II WsE_2/$HfSe_2$ van der waals heterostructure with adjustable electronic and optical properties, Result. Phys. **25**, 104250 (2021).

[91] C. Lei, Y. Ma, X. Xu, T. Zhang, B. Huang, and Y. Dai, Broken-gap type-III band alignment in WtE_2/HfS_2 van der waals heterostructure, J. Phys. Chem. C **123**, 23089 (2019).

[92] D. S. Koda, F. Bechstedt, M. Marques, and L. K. Teles, Trends on band alignments: Validity of Anderson's rule in SnS_2- and $SnSe_2$-based van der Waals heterostructures, Phys. Rev. B **97**, 165402 (2018).

[93] G. Su, V. G. Hadjiev, P. E. Loya, J. Zhang, S. Lei, S. Maharjan, P. Dong, P. M. Ajayan, J. Lou, and H. Peng, Chemical vapor deposition of thin crystals of layered semiconductor SnS_2 for fast photodetection application, Nano Lett. **15**, 506 (2015).

[94] L. Fu, F. Wang, B. Wu, N. Wu, W. Huang, H. Wang, C. Jin, L. Zhuang, J. He, L. Fu, and Y. Liu, Van der waals epitaxial growth of atomic layered HfS_2 crystals for ultrasensitive near-infrared phototransistors, Adv. Mater. **29**, 1700439 (2017).

[95] C. W. Groth, M. Wimmer, A. R. Akhmerov, and X. Waintal, Kwant: A software package for quantum transport, New J. Phys. **16**, 063065 (2014).

[96] T. Kloss, J. Weston, B. Gaury, B. Rossignol, C. Groth, and X. Waintal, Tkwant: A software package for time-dependent quantum transport, New J. Phys. **23**, 023025 (2021).